Late-time X-ray activity from the remnant of GW170817

L. Piro[1], E. Troja[2,3], B. Zhang[4,5,6], G. Ryan[2,14], H. van Eerten[7], R. Ricci[8], M. H. Wieringa[9], A. Tiengo[10,11,12], N. R. Butler[13], S. B. Cenko[3,14], O. D. Fox[15], H. G. Khandrika[15], G. Novara[10,11], T. Sakamoto[16]

[1]*INAF, Istituto di Astrofisica e Planetologia Spaziali, via Fosso del Cavaliere 100, 00133 Rome, Italy*

[2]*Department of Astronomy, University of Maryland, College Park, MD 20742-4111, USA*

[3]*Astrophysics Science Division, NASA Goddard Space Flight Center, 8800 Greenbelt Rd, Greenbelt, MD 20771, USA*

[4]*Department of Physics and Astronomy, University of Nevada, 89154, Las Vegas, NV, USA*

[5]*National Astronomical Observatories, Chinese Academy of Sciences, Beijing 100012, China*

[6]*Department of Astronomy, School of Physics, and Kavli Institute for Astronomy and Astrophysics, Peking University, Beijing 100871, China*

[7]*Department of Physics, University of Bath, Claverton Down, Bath, BA2 7AY, UK*

[8]*INAF-Istituto di Radioastronomia, Via Gobetti 101, I-40129, Bologna, Italy*

[9]*CSIRO Astronomy and Space Science, PO Box 76, Epping, New South Wales 1710, Australia*

[10]*Scuola Universitaria Superiore IUSS Pavia, Piazza della Vittoria 15, 27100 Pavia, Italy*

[11]*INAF - IASF Milano, Via E. Bassini 15, 20133 Milano, Italy*

[12]*Istituto Nazionale di Fisica Nucleare, Sezione di Pavia, Via Bassi 6, 27100 Pavia, Italy*

[13]*School of Earth & Space Exploration, Arizona State University, AZ 85287, USA*

[14]*Joint Space-Science Institute, University of Maryland, College Park, Maryland 20742, USA*

[15]*Space Telescope Science Institute, 3700 San Martin Drive, Baltimore, MD 21218, USA*

[16]*Department of Physics and Mathematics, Aoyama Gakuin University, 5-10-1 Fuchinobe, Chuo-ku, Sagamihara-shi Kanagawa 252-5258, Japan*

Pairs of neutron stars (NSs) are bound to spiral into each other due to their persistent emission of gravitational waves (GWs). Depending on the total mass of the system and the neutron star equation of state, the final product of the NS-NS merger can be either a black hole (BH) or a neutron star. Multi-messenger observations of GW170817[1], the first NS-NS merger system detected by the LIGO/Virgo Collaboration, have shown general consistency with a BH merger product, even though the possibility of a long-lived NS is not ruled out[2, 3]. Here we report the detection of X-ray time variability at $\sim$155 day since the merger with a relative timescale $\Delta t/t \lesssim 0.15$ and amplitude $\Delta F/F \approx 0.7$. Such a feature is analogous to X-ray flares detected in the afterglows of nearly half gamma-ray bursts[4]. Interaction of the relativistic outflow with the surrounding medium cannot easily account for the observed variability[4, 5, 6], which is instead more naturally explained by the late-time activity of the central compact object. At such a late time, an accretion-powered flare[7, 8] from a BH is unlikely. Our results therefore point towards a long-lived neutron star with a strong toroidal but weak poloidal magnetic field[9, 10], which ejects a Poynting-flux-dominated outflow.

Starting on August 26 2017[11], X-ray light from the transient GW170817 is being detected by NASA's Chandra X-ray Observatory and, more recently, by ESA's XMM-Newton satellite. This X-ray emission brightened by a factor of five (Extended Data Figure 1) during the first three months following the NS merger, reaching a luminosity at peak of $\approx 4 \times 10^{39}$ erg s^{-1}. The temporal evolution of the X-ray signal can be described by a power-law rise, $L_X \propto t^{0.8}$, followed by a smooth turn-over $\approx$100 days after the NS merger (Figure 1). The observed emission has been widely interpreted as standard afterglow synchrotron radiation visible across several decades in energy. This broadband radiation is produced by the interaction of a mildly relativistic outflow with a low-density ($n \lesssim 0.01\,\mathrm{cm}^{-2}$) ambient medium, at large radii ($\approx 10^{18}$ cm) from the central power source. The shallow rise and broad peak of the X-ray light curve are at odds with the most common scenario of a collimated outflow with an uniform distribution of energy and Lorentz factors, the so-called top-hat jet. The multi-wavelength dataset requires instead more complex models, such as a significant structure in the energy and velocity angular profiles or a persistent energy injection into the outflow[11, 12, 13]. Both these models can reproduce well the long-term behavior of electromagnetic emission, from radio to X-ray energies (Figure 1 and Extended Data Figure 4).

On top of this overall trend, X-ray monitoring of the source revealed the presence of time variability on a timescale of a few days. Between January 17 and January 28 2018, six consecutive X-ray observations measured a variation of $\approx 1.7 \pm 0.2$ in the X-ray flux (Figure 1, panel b and Extended Data Table 1). By using a simple power-law function as our baseline continuum, we conservatively estimated the significance of this feature as 99.97% (Extended Data Figure 3 and

Methods). A comparable value is derived using theoretical light curves to model the underlying continuum (Figure 1).

X-ray flares are erratic temporal features, commonly seen in GRB afterglows, and often attributed to a re-activation of the central power source[4, 6]. Their emission peaks in the X-ray range, and is often undetected at other energies[14]. Our X-ray observations of GW170817 do not sample the entire temporal profile of the candidate flare, thus preventing a detailed comparison with the population of GRB X-ray flares. Nevertheless, some of its basic properties can be estimated. The similar fluxes measured at 155 and 157 days, followed by a rapid decay phase, suggest that the emission peaked around those dates. The peak time, $t_{pk} \approx 156$ d, and peak luminosity, $L_{pk} \approx 2 \times 10^{39}$ erg s^{-1}, fall within the expected range of values derived by extrapolating the distribution of GRB X-ray flares[15] to later times (Figure 2). We conservatively estimate the flare width as the time interval between the two X-ray observations consistent with the baseline continuum, that is t_1=137 d and t_2=161 d, which yield $\Delta t \lesssim$24 d and $\Delta t/t \lesssim$0.15. The decay phase observed after 157 d places a lower limit of $\Delta t \gtrsim$6 d and $\Delta t/t \gtrsim$0.04. Such rapid variability places our candidate flare in a region that is excluded by most afterglow models[5] (Figure 3 and Methods).

Most naturally, and in analogy with X-ray flares in GRBs, the variability observed in GW170817 is likely related to a central engine that is still active at late times. Strong support to this scenario comes from the so-called "curvature effect" test[16]. Any flare is bound to follow a temporal decay shallower than $\alpha = 2 + \beta$, where $F_\nu \propto t^{-\alpha}\nu^{-\beta}$ and, in our case, $\beta \sim 0.6$[12]. By using the merger time as our reference time T_0, the measured power law decay slope of the flare is $\alpha \sim 9.9$, greater

than the predicted value. This is likely due to a mis-identified zero time T_0[6]. By imposing that $\alpha = 2 + \beta \sim$2.6 and fitting for T_0, we find that T_0 is 116^{+11}_{-26} d consistent with the hypothesis that the central engine was reactivated at late times.

GW observations constrain the mass of the remnant to $< 2.8\ M_\odot$, but do not break the degeneracy between a NS and a BH[2]. If the final merger product is a BH, then its re-activation could be due to either fallback accretion[7] or disc fragmentation[8]. In the former scenario, the total fallback power declines as $t^{-5/3}$ and, for typical ejecta masses of NS mergers, is $\lesssim 10^{39}$ erg s^{-1} at 160 d after the merger. This is comparable to the observed X-ray luminosity, and would therefore require an unrealistic radiative efficiency in order to accommodate our observations. The latter scenario needs the accretion disc to survive for months, which is not expected based on our understanding of NS mergers[8].

Depending on the unknown NS equation of state, a supra-massive (supported by rigid rotation) or even a permanently stable NS can survive after the merger. Due to its rapid differential rotation, this post-merger NS likely has a strong toroidal component of the magnetic field and possibly also a strong poloidal component[17]. The untwisting of the toroidal magnetic field may give rise to an abrupt injection of outflows with enhanced wind luminosity, and the internal magnetic dissipation of such an outflow[18] would give rise to flaring emission observable in X-rays, with a mechanism similar to GRB X-ray flares [19] or bursts and flares of soft gamma-ray repeaters[20] (SGRs). We estimate the toroidal component of the magnetic field as follows. The total isotropic-equivalent energy of the flare is in the range $7 \times 10^{44}\ \mathrm{erg} < E_{\rm flare} < 3 \times 10^{45}\ \mathrm{erg}$. This is much

smaller than the total spin energy of a new-born millisecond pulsar. If one exclusively attributes the flare energy to the NS magnetic field energy, then $B^2R^3/6 \gtrsim 3\times10^{45}$ erg. Therefore, the required toroidal magnetic field stored in the NS must be $B_{\rm t} \gtrsim 10^{14}$ G, which is reasonably expected[17].

In order to accommodate the available electromagnetic observations, the merger product should have a weak poloidal magnetic field[21, 3]. During the spin-down process (either due to magnetic dipolar radiation or secular GW radiation), a continuous Poynting-flux-dominated outflow is launched and adds energy into the ejecta. The dipolar poloidal magnetic field at the NS surface should be below $\approx 10^{12}$ G in order to satisfy the upper limits set by the broadband observations, including the prompt γ-rays, the kilonova emission and the long-term X-ray, optical, and radio afterglow[3]. Such a high-toroidal-B and low-poloidal-B NS is analogous to the source SGR 0418+5729 that emits magnetar flares[10] but has a dipolar magnetic field[9] lower than 7.5×10^{12} G.

A long-lived NS is not only allowed, but is also helpful to interpret some of the data. The remnant NS deposits extra energy to power the kilonova emission[22, 23]. This helps to account for the early peak and high luminosity of the "blue kilonova"[21], otherwise difficult to explain with standard model parameters[11, 24]. Indeed, a NS with initial spin-down luminosity of $\sim 3.4\times10^{44}\ {\rm erg\ s^{-1}}$ at 500 s and a luminosity evolution $\propto t^{-1}$ (gravitational wave spindown dominated regime) can account for the multi-wavelength evolution of AT2017gfo without the need of introducing a large amount of ejecta mass and an unreasonably small opacity[24]. With these parameters, the spin-down luminosity at ~ 1 day is $\sim 2\times10^{42}\ {\rm erg\ s^{-1}}$, too low to significantly affect the opacity of the merger ejecta[25]. This satisfies the observational constraint of a "red kilonova" component as well as the

spectral features of lanthanides elements[26, 11].

If the remnant of GW170817 is a long-lived NS, then the maximum mass of a non-spinning NS should be greater than $2.16M_{\odot}$[27], superseding the current lower limit of $2M_{\odot}$ set by PSR J1614-2230[28]. This new limit would eliminate essentially all the soft neutron star equations of state invoking hyperons and boson condensation[29] and supports the suggestion[30] that a good fraction of NS-NS mergers leave behind supra-massive or stable NSs.

Acknowledgements

This work was partially supported by NASA through grants issued by the Chandra X-ray Observatory Center and the Space Telescope Science Institute.

Author Contributions

LP, ET, BZ, GR, and HvE composed the text based on inputs from all the co-authors. BZ developed the NS model. GR and HvE developed the jet and cocoon models, and led the modeling of the afterglow emission. LP, ET, AT, and GN obtained, processed and analyzed the X-ray observations. ET, RR, and MHW obtained, processed and analyzed the ATCA observations. ET, NRB, ODF, and HGK obtained, processed and analyzed the HST observations. All authors discussed the results and commented on the manuscript.

Author Information

Reprints and permissions information is available at www.nature.com/reprints. The authors declare no competing financial interests. Correspondence and requests for materials should be addressed to LP (luigi.piro@iaps.inaf.it)

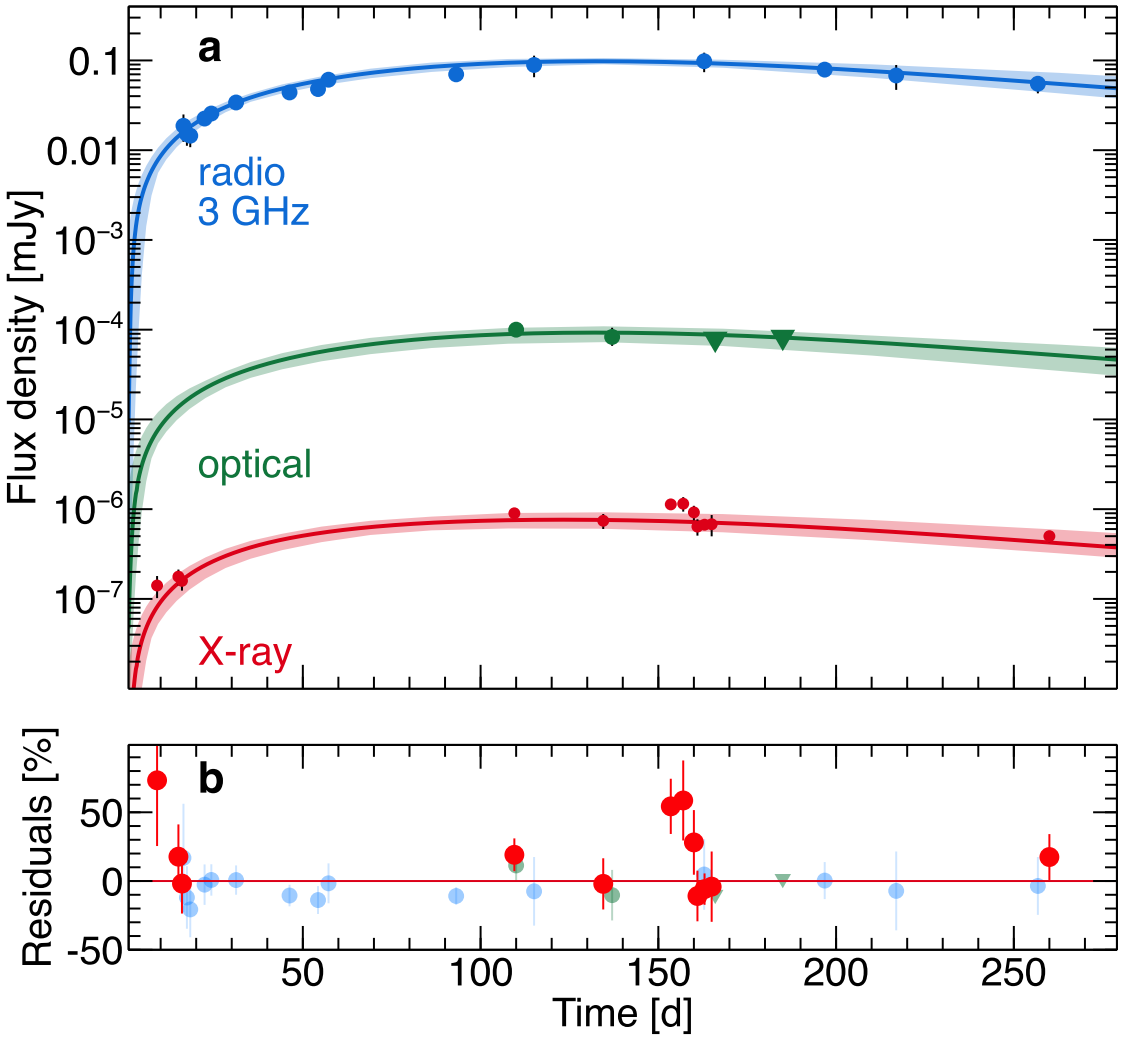

Figure 1 Afterglow temporal evolution for GW170817. **a** The multi-wavelength dataset is compared with theoretical jet models (solid lines). The width of each model curve indicates the 68% range of confidence. **b** The X-ray residuals show a temporal feature at ≈155 d after the merger. Vertical error bars are 1 σ. Upper limits (downward triangles) are 3 σ.

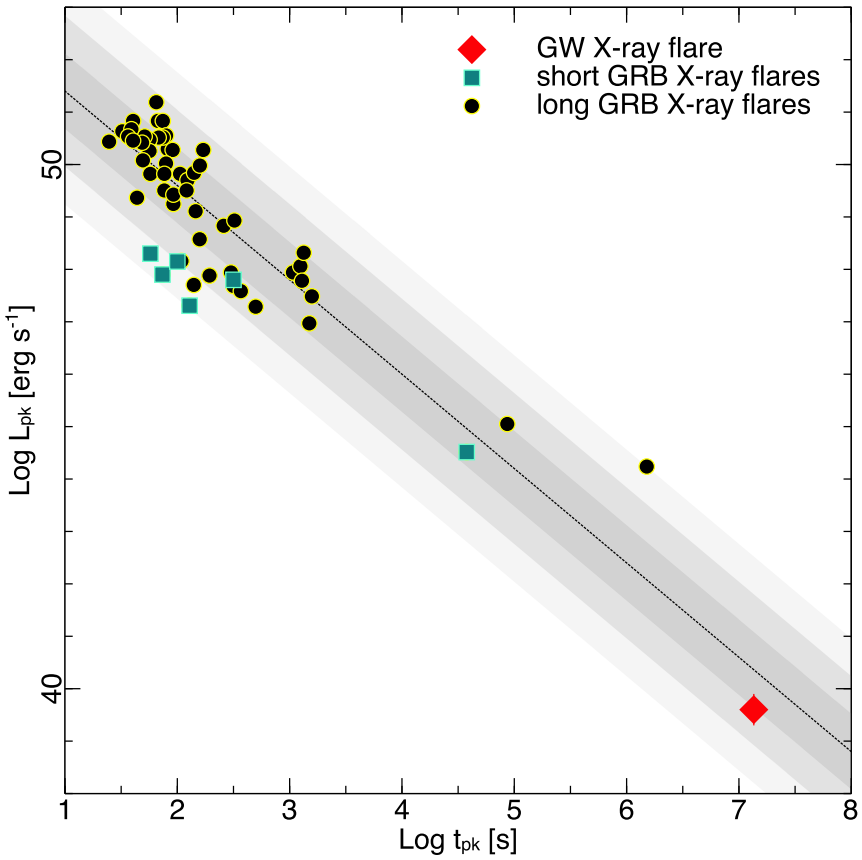

Figure 2 Comparison with X-ray flares in GRB afterglows. The luminosity and peak time of the candidate X-ray flare in GW170817 (red diamond) follow the trend observed in GRB X-ray flares. The best-fit relation for GRB X-ray flares[15] is shown by the dashed line. The shaded areas shows the 1 σ (dark grey), 2 σ and 3 σ (light grey) regions.

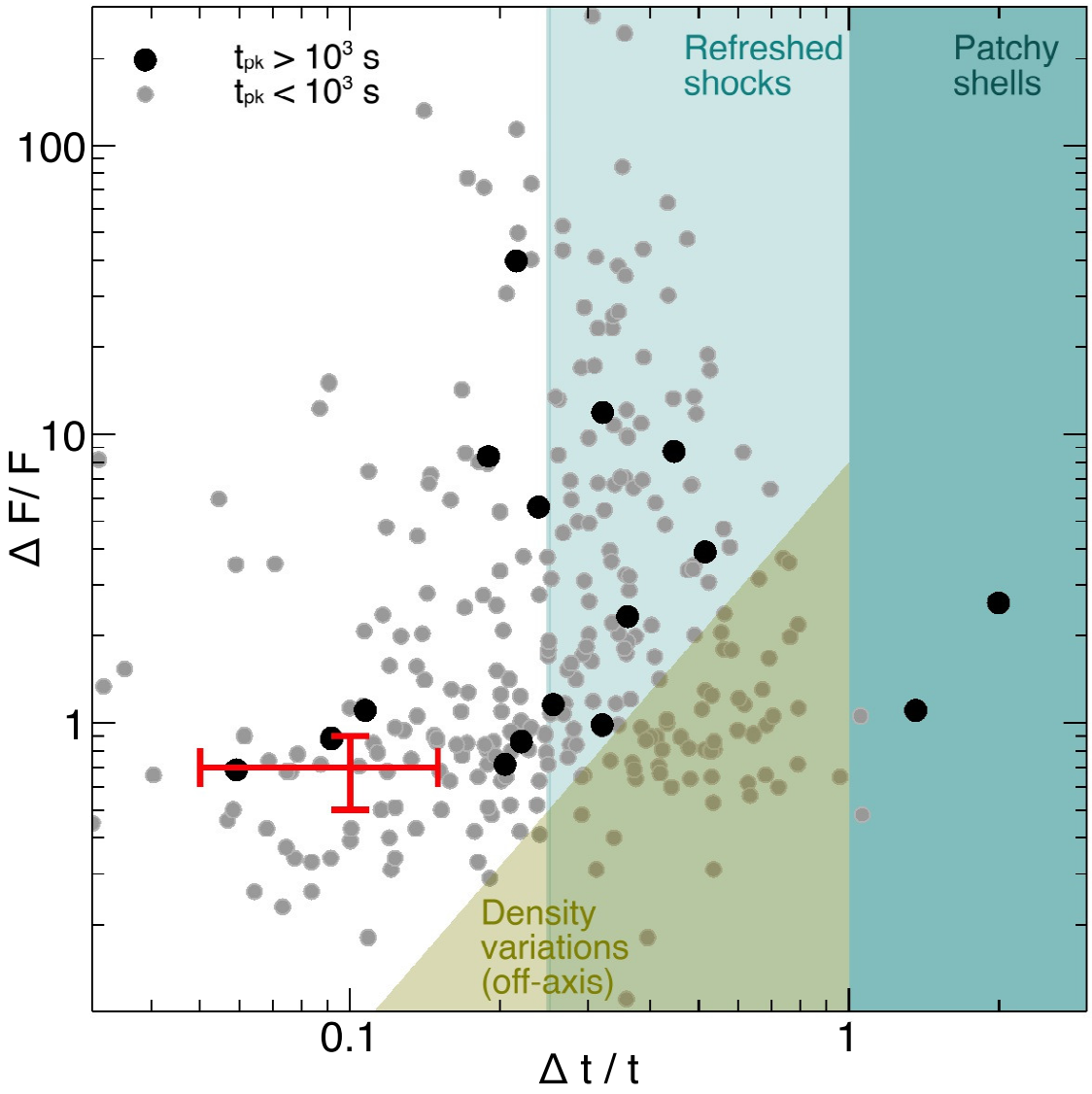

Figure 3 Ioka diagram for X-ray flares. X-ray flares in GRBs (circles) and GW170817 (red data point) are shown. The horizontal error bar reports the uncertainty in the flare duration due to the sparse sampling. The shaded areas show the regions allowed by afterglow models[5]. Most X-ray flares, including the one observed in GW170817, lie outside these regions.

Extended Data Table 1 Late time X-ray observations of GW170817. Errors are 1 σ.

$T - T_0$ (d)	Exposure (ks)	Unabsorbed Flux (10^{-14} erg cm^{-2} s^{-1})	Energy band (keV)	Facility
153	32.1	3.2 ± 0.4	0.3–10	*Chandra*
157	16.0	3.2 ± 0.6	”	”
160	21.0	2.6 ± 0.5	”	”
161	22.5	1.8 ± 0.4	”	”
163	110	1.9 ± 0.2	”	*XMM-Newton*
165	14.4	1.9 ± 0.5	”	*Chandra*
260	96.8	1.4 ± 0.2	”	”

Extended Data Table 2 Late time HST observations of GW170817. Upper limits are 3 σ. Magnitudes are corrected for Galactic extinction using E(B–V)=0.105[31].

$T - T_0$ (d)	Instrument	Filter	Exposure (s)	AB mag
110	WFC3/UVIS	F814W	2400	26.4 ± 0.2
166	WFC3/UVIS	F606W	2372	<26.7
209	WFC3/UVIS	F606W	2432	<26.6

Extended Data Table 3 Late time ATCA observations of GW170817. Errors are 1 σ. Upper limits are 3 σ.

$T - T_0$ (d)	Frequency (GHz)	Bandwidth (GHz)	Configuration	Exposure (hrs)	Flux (μJy)
125	5.5	2.0	6C	10.5	72 ± 9
	9.0	2.0	6C	”	72 ± 9
149	5.5	2.0	6C	10.5	79 ± 8
	9.0	2.0	6C	”	50 ± 7
160	19	4.0	750A	10.5	< 36
169	5.5	2.0	750A	6.5	< 87
	9.0	2.0	750A	”	< 126
182	5.5	2.0	750B	9.5	81 ± 16
	9.0	2.0	750B	”	54 ± 11

Extended Data Table 4 Constraints on the relativistic outflow of GW170817. Parameters are listed for both the Gaussian Jet and the Cocoon models. Reported are the median values of each parameter's posterior distribution with symmetric 68% uncertainties (i.e. the 16% and 84% quantiles).

	Gaussian Jet		Isotropic Cocoon
Parameter	Fit result	Parameter	Fit Results
θ_v (rad)	$0.58^{+0.15}_{-0.16}$	$\log_{10} u_{\rm max}/c$	$1.57^{+0.86}_{-0.70}$
$\log_{10} E_0/{\rm erg}$	$52.33^{+0.83}_{-0.54}$	$\log_{10} u_{\rm min}/c$	$0.60^{+0.44}_{-0.41}$
θ_c (rad)	$0.090^{+0.024}_{-0.025}$	$\log_{10} E_{\rm inj}/{\rm erg}$	$56.8^{+3.9}_{-3.8}$
θ_w (rad)	$0.83^{+0.46}_{-0.41}$	k	$7.22^{+0.41}_{-0.51}$
		$\log_{10} M_{\rm ej}/M_\odot$	$-8.2^{+2.0}_{-1.3}$
$\log_{10} n_0/{\rm cm}^{-3}$	$-1.62^{+0.77}_{-0.93}$	$\log_{10} n_0/{\rm cm}^{-3}$	$-5.1^{+2.8}_{-2.7}$
p	$2.1697^{+0.0097}_{-0.018}$	p	$2.1793^{+0.068}_{-0.010}$
$\log_{10} \epsilon_e$	$-1.12^{+0.55}_{-0.90}$	$\log_{10} \epsilon_e$	$-2.2^{+1.4}_{-1.2}$
$\log_{10} \epsilon_B$	$-4.09^{+0.88}_{-0.64}$	$\log_{10} \epsilon_B$	$-3.1^{+1.7}_{-1.4}$
$\log_{10} E_{tot}/{\rm erg}$	$50.21^{+0.78}_{-0.48}$	$\log_{10} E_{tot}/{\rm erg}$	$52.6^{+1.2}_{-1.4}$

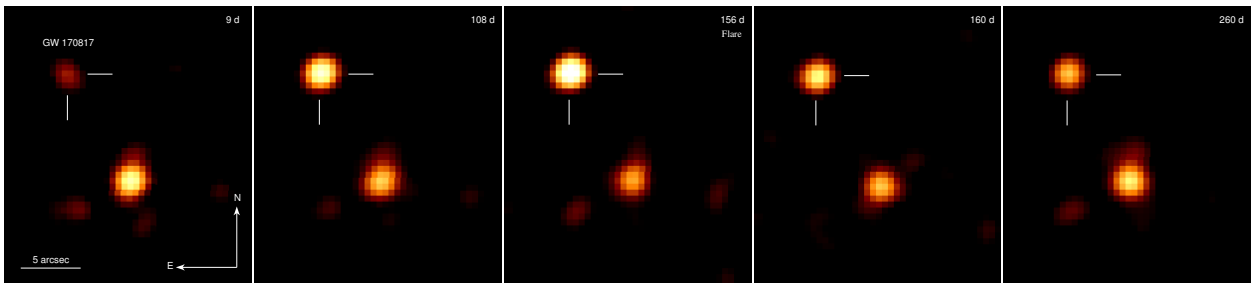

Extended Data Figure 1 X-ray afterglow of GW170817. Images are background subtracted, corrected for exposure, and smoothed with a Gaussian function with σ=1.5″. The X-ray emission from GW170817 is seen to slowly evolve with time. However, a rapid decrease in brightness is observed between 156d and 160d after the NS merger. During this interval, the X-ray count rate decreases by a factor of 1.7. Between 160 d and 260 d, it decreases by a factor of 1.3.

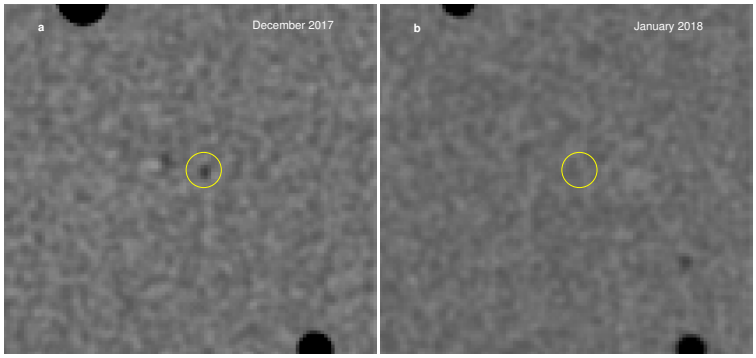

Extended Data Figure 2 Optical afterglow of GW170817. Images are galaxy subtracted and smoothed with a Gaussian function. The optical afterglow from GW170817 (yellow circle) fades between the two HST epochs, carried at 110 d and 160d after the NS merger, respectively.

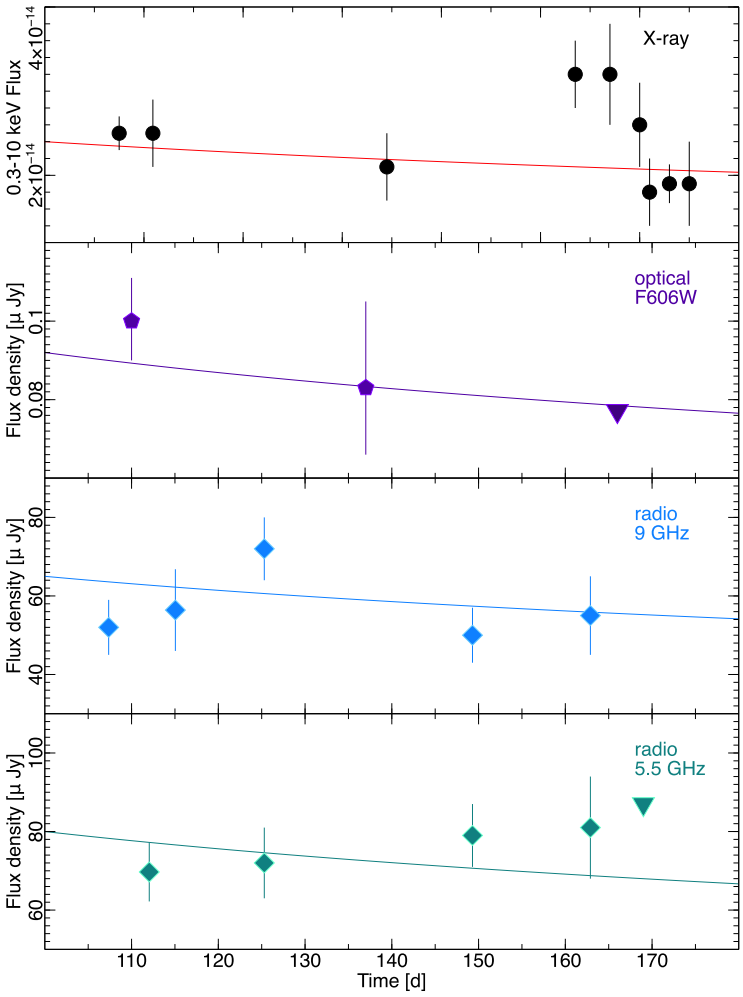

Extended Data Figure 3 Multi-wavelength afterglow of GW170817. This zoom-in shows the afterglow light curves at different energies around the peak time. The solid lines show our best estimate of the underlying continuum used to derive the significance of the candidate flare.

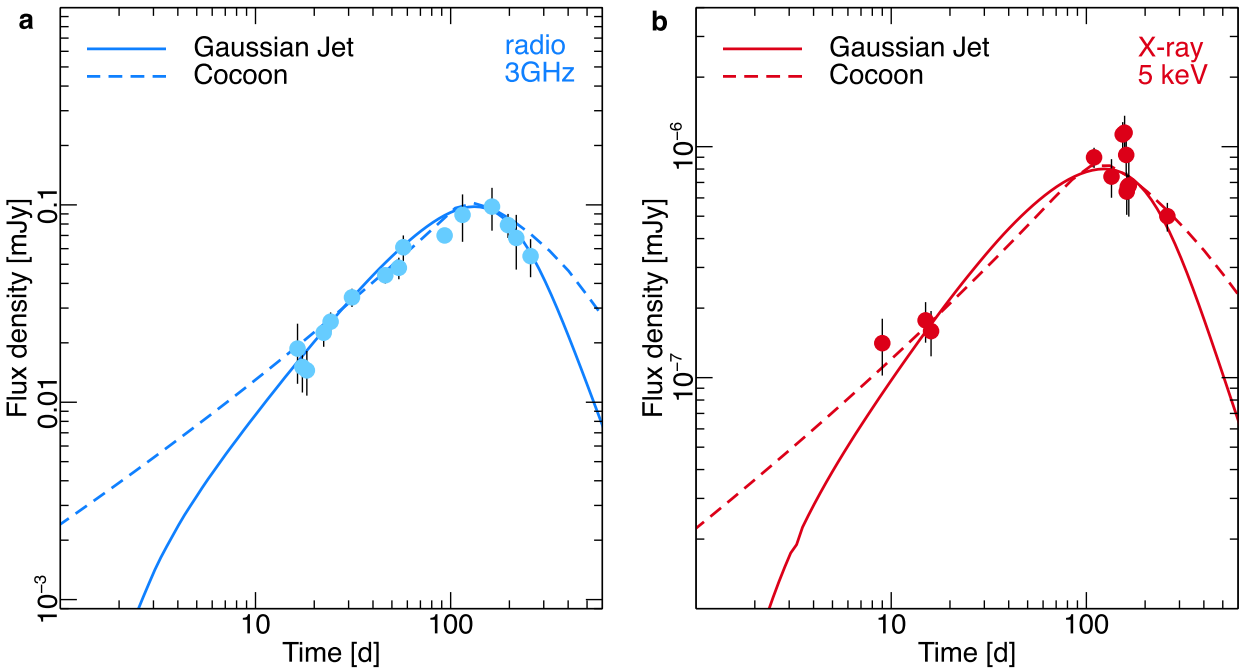

188

189

190 **Extended Data Figure 4 Comparison between the Jet and Cocoon models. a** The

191 radio dataset is well described by either a Gaussian jet (solid line) or by an isotropic

192 cocoon (dashed line). **b** Same as in a, for the X-ray data set.

193 **METHODS**

194 **X-ray observations**

195 A log of X-ray observations around the flare is reported in Extended Data Table . Earlier observa-
196 tions were reported in [11, 12, 32, 33]. *Chandra* data were reduced in a standard fashion using the CIAO
197 v4.9 and the latest calibration files. Source counts were extracted from a circular region containing
198 92% of the encircled energy fraction, whereas the background contribution was estimated from
199 nearby source-free regions. We verified that none of the observations was affected by high levels
200 of particle background.

201 *XMM-Newton* data were processed using SAS v16.1.0 and the most recent calibration files.
202 Periods of high background were excluded from the analysis. The native astrometry was refined
203 by matching the positions of 5 bright X-ray sources with their optical counterparts in the GSC
204 v2.3.2 catalogue[34]. In order to minimize the contribution from contaminating X-ray sources, a
205 small aperture of 5" was used to extract the source counts.

206 X-ray spectra were binned in order to have at least one count per energy channel and fit
207 within the XSPEC v12.8.2 package by minimizing the C-statistics. To convert the observed count-
208 rates to flux values we adopted a spectral index $\beta = 0.575$ as derived from the broadband spectral
209 energy distribution [12].

Optical observations

We obtained two late-time epochs of imaging (PI: Troja) with the Hubble Space Telescope. Images were taken with the UVIS detectors of the Wide-Field Camera 3 (WFC3). Data were reduced in a standard fashion using the Hubble Space Telescope CalWF3 standard pipeline[35], and the astrodrizzle processing[36]. We followed the same procedure of [11] to create a galaxy template, and subtracted it to each image. We tested our method on earlier HST observations[37] and successfully recovered the optical transient (Extended Data Figure 2). However, in our later images the afterglow is no longer visible. This rules out the model by [38] which predicts a continued rise of the afterglow up to 150 d. Fluxes were converted to magnitudes using WFC3 zero points. Our final photometry is listed in Extended Data Table and shown in Figure 1. Earlier observations are reported in [37, 39].

Radio observations

The target source was observed with the Australia Telescope Compact Array (ATCA) at five different epochs under programs CX394 (PI: Troja) and CX391 (PI: Murphy). In order to bootstrap the flux density scale the standard source 1934-638 was observed in all epochs. The phase calibrators 1245-197 (first two epochs) and 1244-255 (last three epochs) were used to compute the complex gains. All the data sets were flagged, calibrated and imaged using standard procedures in the data reduction package MIRIAD. In order to maximize the results the 5.5 and 9 GHz data were imaged using a robustness parameter value of r=0.5 (1st and 2nd epochs) and r=-0.5 (4th and 5th epochs). Flux measurements for all epochs are reported in Extended Data Table. Data from previous epochs

are from [13, 12, 39].

Temporal analysis

At late times radio, optical, and X-ray emission belong to the same synchrotron segment [12]. We therefore modeled the multi-wavelength light curves around the time of the candidate flare by imposing that they follow the same temporal decay. As the initial fit was poor (P-value $<5\%$), we removed the data point with the largest positive residual from the fit and iteratively repeated this process until P-value$>5\%$. The resulting best-fit model was selected as our baseline continuum (solid line in Extended Data Figure 3) and the candidate flaring component was identified as an excess above this model. This procedure is similar to the one used to identify flares in GRB afterglows [40]. In order to estimate the significance of this excess, we ran a set of 10,000 Monte Carlo simulations. We used our best-fit continuum as template model and repeated the same search procedure on the simulated light curves. From this method we derived a probability of $\approx 3 \times 10^{-4}$ to identify a statistical fluctuation as a flaring component.

Modelling of the outflow: jet and cocoon

The extended power-law rise exhibited by the GW170817 afterglow light curve can not be produced by a simple top-hat jet model[13, 12]. This phase requires additional structure in the outflow: an angularly dependent energy profile, a radial stratification of velocities, or some combination[41, 42, 43]. Following [12] we consider two representative models: a *structured jet* with Gaussian angular energy profile, and an isotropic *cocoon* with radial velocity stratification. To fit each model we perform

Bayesian parameter estimation by sampling the posterior probability distribution with a Markov-Chain Monte Carlo (MCMC) package[44].

The Gaussian jet assumes an energy profile $E_0 \exp[-\theta^2/2\theta_c^2]$, up to a truncation angle θ_w, imprinted on the jet either through the launching mechanism or its interaction with its immediate environment. There is no current consensus on the exact angular energy distribution within short GRB blast waves, and this parametrization is to be taken as a representative stand-in for a range of models with steeply dropping energies around a central core.

The cocoon is an isotropic outflow whose energy is distributed among velocities according to $E_{>u}(u) = E_{inj} u^{-k}$, where $u \, \epsilon \, [u_{min}, u_{max}]$ is the four-velocity[13]. Slow material is incorporated into the forward shock as it decelerates, increasing its energy and brightening the emission. We take the initial fast outflow to have a total mass M_{ej}.

Our representative cocoon and Gaussian jet models represent extreme cases on the spectrum of angular energy distribution profiles. A GRB outflow embedded in a cocoon, even in the case of a failed GRB, can exhibit angular anisotropy and effectively resemble a Gaussian jet. More generally, the structure of a Gaussian jet might reflect this cocoon component, but can also be produced in the absence of a dense cocoon-forming environment by the jet-torus interaction during launching [45].

Each blast wave model propagates through an environment of constant number density n. We calculate the ensuing synchrotron radiation from (trans-)relativistic ejecta [46], with $-p$ the power-

law slope of accelerated electrons, ε_e, the fraction of post-shock internal energy in the accelerated electrons, and ε_B the fraction of post-shock internal energy residing in shock-generated magnetic field that is assumed without preferred direction on macroscopic scales.

In the Gaussian jet model, θ_ν is the orientation of the jet axis relative to the observer. Because this inclination angle has also been constrained directly from the GW measurement [47], we include fit results for multiple options on the prior of θ_ν. As in [12], these are a default option of $p(\theta_\nu) \propto \sin\theta_\nu$, a version utilizing the gravitational wave data together with a Hubble constant value from SH_0ES [48], and a version where the Hubble constant is determined from Planck data [49].

Constraints on the outflow

The results of the MCMC analysis are summarized in Extended Data Table 4. Two runs are presented: the Gaussian jet and the quasi-isotropic cocoon (Extended Data Figure 4) well describe the dataset up to 260 d after the merger. The three X-ray observations identified as part of the flare are not included in the fit. When these data are included the conclusions about the model parameters do not significantly change.

The Gaussian jet has a well constrained opening angle $\theta_c = 0.09 \pm 0.02$ rad (5.2°), and a total energy of the order 10^{50}erg. The viewing angle of 0.6 rad (34°) is consistent with the LIGO estimates that also informed the prior. The Gaussian jet wide truncation angle is largely unconstrained, and the micro-physical parameters are constrained around $\epsilon_e \sim 0.1$ and $\epsilon_B \sim 10^{-4}$. The ISM number density is constrained at $\approx 10^{-2}$ cm^{-3}.

The isotropic (cocoon) model requires a small amount of relativistic ejecta with a substantial Lorentz factor $\Gamma_{max} \in [7.5, 270]$ (68% percent) followed by an energetic tail of slower ejecta. The slow ejecta has a minimum Lorentz factor $\Gamma_{min} \in [1.8, 11]$. The total energy, assuming a spherical blast wave, is $10^{52.6\pm1.3}$ erg. The ISM density is poorly constrained to $10^{-5\pm3}$ cm^{-3}. The synchrotron parameters ϵ_e and ϵ_B are very poorly constrained to $10^{-2.2\pm1.3}$ and $10^{-3\pm1.5}$ respectively. The high Lorentz factors necessary for the isotropic model are in tension with a choked-jet scenario, where the ejecta achieve only Newtonian velocity.

Late time central engine activity may inject energy into the afterglow blast wave, altering the evolution of the forward shock and the ensuing electromagnetic emission. We expanded the Gaussian jet model to include isotropic energy injection of the form $L(t) = L_0(t/t_0)^{-q}$ until a stop time t_s. When included in an MCMC run, we find the energy injection must be a sub-dominant component and obtain an upper limit $L_0 < 4 \times 10^{44}$ erg/s with 95% confidence. The q and t_s parameters are unconstrained, and the other parameters of the jet are unchanged from the values in Extended Data Table 4. The luminosity required to produce the x-ray flare is comfortably within this constraints.

The observed light curves and spectra show no clear sign of electron cooling, and our models put the synchrotron cooling break near or well above the X-ray band. Note that the synchrotron cooling break is intrinsically smooth, and would not stand out strongly even if occurring within the X-ray band. Furthermore, equating electron cooling and acceleration time scales provides an estimate for the upper cut-off in synchrotron emission that lies above the X-ray band as well. This

feature is therefore also not directly constrained by the broadband observations, which predominantly cover a single spectral regime between the synchrotron injection and cooling breaks.

Origin of the X-ray variability: afterglow

The rapid variability $\Delta t/t \lesssim 0.15$ places our candidate flare in a region excluded by afterglow models[5, 50, 51] (Figure 3). At 160 d the forward shock is still moving at a mildly relativistic velocity. The light crossing time across the shock front is then of the same order as the time since the explosion, i.e. $\Delta t \approx t$, much longer than observed. In principle a small region of angular size $\Delta\theta$ such that $\Delta t \gtrsim R\Delta\theta \max(\Delta\theta/2, 2\theta_v)/c$ can accomodate the observed timescale [5]. However, it has been demonstrated both analytically and numerically that, even for strong density perturbations, flux changes are smoothed over much longer time scales [52, 53, 54]. A further argument is the following. By taking into account the volume of the variable region and the volume of the observable region one derives an upper limit

$$\Delta F_\nu/F_\nu \lesssim \begin{cases} 4/5\ \Delta t/t\ f_{enhance} & (\mathrm{on-axis}) \\ 6(\Delta t/t)^2\ f_{enhance} & (\mathrm{off-axis}) \end{cases} \quad (1)$$

where the enhancement due to a overdensity n_f is $f_{enhance} = (\nu_{c,f}/\nu_c)^{-1/2} - 1 = (n_f/n)^{1/2} - 1$, where $\nu_{c,f}$ is the cooling frequency of the blob. When the density increases as much as to shift the cooling frequency below the observed frequency, there is no longer a gain and the flux remains constant. Thus the maximum gain is $f_{enhance} \approx (\nu_c/\nu_x)^{1/2}$. From eq. 1, in order to satisfy the flare properties requires $\nu_c \gtrsim 10^{21}$ Hz. This is not consistent with the value derived for the structured jet model and would require an unplausible low density of the ISM $n \lesssim 10^{-7}$ cm^{-3} for the cocoon

model. This value is lower than the density external to galaxies, that ranges from $\approx 10^{-3}$cm^{-3} in clusters of galaxies to $\gtrsim 10^{-6}$cm^{-3} in cosmological filaments [55].

In the case of a cocoon, where energy injection by an outflow with a spread of Lorentz factors drives the shock, a strong modulation of the profile over the assumed power-law can produce a bump in the light curve when e.g. a massive late relativistic shell catches up with the shock front. However this interaction will produce bumps that have typically $\Delta t \approx t$, thus much longer than observed. In addition the predicted stepwise increase above the baseline does not reproduce the observed flare-like feature. In the case of a structured jet while the broader and slower component will quickly lose its energy in the environment, the (faster) narrow-core of the jet will excavate a free path to the slower ejecta in its wave, thus allowing $\Delta t \ll t$ [56]. However, as in the previous case, a stepwise light curve is expected. Finally, a structured jet with a significant angular structure (patchy jet) would also give a similar variability time scale $\Delta t \approx t$, and therefore disfavored.

Origin of the X-ray flare: central engine

Since the $\alpha = 2 + \beta$ "curvature effect" test [57, 16] works well for the flare, the X-ray emission likely originates from a radius $R_{\rm flare} \sim \Gamma^2_{\rm flare} c \Delta t_{\rm decay} \sim (2.6\times10^{18}\ {\rm cm})(\Gamma_{\rm flare}/10)^2(\Delta t_{\rm decay}/10\,{\rm d})$, where $\Delta t_{\rm decay} \sim 10$ d is the decay time scale of the flare. At ~ 150 d after the merger, the external shock blastwave has moved to a distance $R_{\rm blast} \sim \Gamma^2_{\rm blast} ct \sim (6.2 \times 10^{18}\ {\rm cm})(\Gamma_{\rm blast}/2)^2(t/150\,{\rm d})$ from the central engine. Therefore the flare emission is "internal" if the Lorentz factor of the emitting material is ≈ 10. This is consistent with various constraints that GRB X-ray flares have a lower

Lorentz factor than GRB themselves [58]. The trigger of the flare may be through collision-induced magnetic reconnection and turbulence [18, 59] or an external-pressure triggered kink instability [60]. Either way, an enhanced release of the Poynting flux energy due to reconnection is induced, giving rise to the flare emission.

The emitting region is outside the radius of the non-relativistic merger ejecta, $R_{ej} \lesssim 1.2\,10^{17}(\beta/0.3)(t/150d$ This is because in the observer's viewing direction, there is already a funnel opened by the earlier relativistic ejecta that powered the prompt emission of GRB 170817A. With continuous energy injection from a spinning-down NS, the funnel would remain open so that the newly ejected enhanced Poynting flux can penetrate through the ejecta and reach the large radius where X-ray emission is released. This can be seen from the following estimates:

In order to see whether the funnel remains open, one can compare the pressure of the ejecta and the comoving-frame magnetic pressure of the pulsar wind. Suppose that the central engine spindown luminosity evolves with time as

$$L(t) \propto t^{-q}, \tag{2}$$

the comoving-frame magnetic field strength of the pulsar wind may be estimated as $B' \propto L^{1/2}R^{-1}\Gamma^{-1}$, so that the magnetic pressure scales as $p_B = B^2/8\pi \propto t^{-q}R^{-2}$ (assuming Γ does not evolve significantly with time). The gas pressure of the ejecta, on the other hand, scales as $p \propto \rho^{5/3} \propto R^{-10/3} \propto t^{-10/3}$ assuming adiabatic evolution and no radial spreading of the ejecta. Radiative loss and radial spreading would further steepen the decay. We consider the competition between p_B and p at the radius of the ejecta, so that $R \propto t$. One can then compare $p_B \propto t^{-(2+q)}$ and $p \propto t^{-10/3}$.

For a low-B pulsar, the spindown time scale is long. One may make a connection between the spindown time scale and the turn-over time of X-ray emission (~ 160 d). Before this time, one has q either 0 (dipole-spindown-dominated) or 1 (secular-GW-spindown-dominated). For both cases (and any intermediate value of q), the decay slope of p_B is shallower than the decay slope of p. This suggests that the funnel would remain open, and likely would widen as a function of time.

In order to power an X-ray flare ~ 150 d after the merger, the central engine needs to be a supramassive or even stable NS that survived at least such a long duration of time. Previous criticisms to such a long-lived remnant include the moderate kinetic energy in the kilonova and afterglow as well as the the apparent difficulty of producing a short GRB in a neutron star engine [61, 62]. On the other hand, a neutron star with a low poloidal magnetic field and strong toroidal field (and hence, a large ellipticity to allow significant gravitational wave spindown loss) is allowed by the data [3], and energy injection to the kilonova from such a remnant indeed helps to interpret the kilonova properties without invoking extreme parameters [63, 24]. Furthermore, mechanisms to produce a short GRB in a neutron star central engine without the introduction of a black hole have been discussed in the literature, including early accretion [64] or magnetic activities due to differential rotation [65]. A good fraction of short GRBs are found to possess an extended "internal plateau", which suggested the existence of a supra-massive or stable neutron star [66, 67]. Interpreting these features within the neutron star engine model indeed require significant energy loss in the gravitational wave channel [30], which is consistent with the model requirement presented here.

Energy injection from the pulsar

The existence of a central engine pulsar would inevitably provide additional energy injection to the blastwave and to the kilonova ejecta. This would influence the emission properties of the broad-band afterglow and the kilonova emission. Energy injection into a blastwave by an underlying pulsar has been extensively studied [68, 69]. For an engine satisfying Eq.(2), in the spectral regime below ν_c (where the X-rays seem to lie in), the forward shock flux scales as [69, 6]

$$F_\nu \propto t^{(1-q)-\frac{(p-1)(2+q)}{4}}, \tag{3}$$

which is valid for $q \leq 1$. The broad-band afterglow spectral index of GW170817 suggests $p \sim 2.2$. The observed $F_\nu \propto t^{0.8}$ rise of the afterglow demands $q \sim -0.29$, which is out the scope of the pulsar model. This suggests that energy injection of the pulsar can at most partially contribute to the observed energy injection of GW170817 afterglow. Additional energy injection, either from high latitudes of a structured jet or from a stratified ejecta outflow (in the cocoon scenario), is needed. For $q = 1$ (relevant for secular-GW-spindown-dominated case), energy injection is essentially negligible. The energy injection parameters from the two models (structured jet and cocoon) are essentially the same as the ones without invoking central engine energy injection. For $q = 0$ (relevant for dipolar-spindown-dominated phase), the engine injection from the pulsar does not alter the afterglow emission provided $L_0 < 4\times10^{44}$erg/s as demonstrated previously. The inclusion of reverse shock emission can also interpret the broad-band data.[70]

The impact on the kilonova due to the energy injection of the underlying pulsar has been studied [63, 24]. Both the early (blue) and late (red) kilonova components can be accounted for with

reasonable values of ejected mass and opacity if the neutron star spindown is dominated by gravitational wave losses. [24] For such a case, energy injection into the blastwave due to central engine is negligibly small, which does not affect the best MCMC fitting parameters presented in §.

Data availability: All relevant data are available from the corresponding author upon reasonable request.

1. Abbott, B. P. *et al.* Multi-messenger Observations of a Binary Neutron Star Merger. ApJ **848**, L12 (2017).

2. Abbott, B. P. *et al.* Search for Post-merger Gravitational Waves from the Remnant of the Binary Neutron Star Merger GW170817. ApJ **851**, L16 (2017). 1710.09320.

3. Ai, S. *et al.* The allowed parameter space of a long-lived neutron star as the merger remnant of GW170817. *ArXiv e-prints, arXiv:1802.00571* (2018). 1802.00571.

4. Chincarini, G. *et al.* The First Survey of X-Ray Flares from Gamma-Ray Bursts Observed by Swift: Temporal Properties and Morphology. ApJ **671**, 1903–1920 (2007). astro-ph/0702371.

5. Ioka, K., Kobayashi, S. & Zhang, B. Variabilities of Gamma-Ray Burst Afterglows: Long-acting Engine, Anisotropic Jet, or Many Fluctuating Regions? ApJ **631**, 429–434 (2005). astro-ph/0409376.

6. Zhang, B. *et al.* Physical Processes Shaping Gamma-Ray Burst X-Ray Afterglow Light Curves: Theoretical Implications from the Swift X-Ray Telescope Observations. ApJ **642**, 354–370 (2006). arXiv:astro-ph/0508321.

7. Rosswog, S. Fallback accretion in the aftermath of a compact binary merger. MNRAS **376**, L48–L51 (2007). astro-ph/0611440.

8. Perna, R., Armitage, P. J. & Zhang, B. Flares in Long and Short Gamma-Ray Bursts: A Common Origin in a Hyperaccreting Accretion Disk. ApJ **636**, L29–L32 (2006). astro-ph/0511506.

9. Rea, N. *et al.* A Low-Magnetic-Field Soft Gamma Repeater. *Science* **330**, 944 (2010). 1010.2781.

10. Tiengo, A. *et al.* A variable absorption feature in the X-ray spectrum of a magnetar. Nature **500**, 312–314 (2013). 1308.4987.

11. Troja, E. *et al.* The X-ray counterpart to the gravitational-wave event GW170817. Nature **551**, 71–74 (2017). 1710.05433.

12. Troja, E. *et al.* The outflow structure of GW170817 from late time broadband observations. *ArXiv e-prints* (2018). 1801.06516.

13. Mooley, K. P. *et al.* A mildly relativistic wide-angle outflow in the neutron-star merger event GW170817. Nature **554**, 207–210 (2018). 1711.11573.

14. Troja, E. *et al.* Swift and Fermi Observations of X-Ray Flares: The Case of Late Internal Shock. ApJ **803**, 10 (2015). 1411.1415.

15. Bernardini, M. G., Margutti, R., Chincarini, G., Guidorzi, C. & Mao, J. Gamma-ray burst long lasting X-ray flaring activity. A&A **526**, A27 (2011). 1004.3831.

16. Liang, E. W. *et al.* Testing the Curvature Effect and Internal Origin of Gamma-Ray Burst Prompt Emissions and X-Ray Flares with Swift Data. ApJ **646**, 351–357 (2006). arXiv:astro-ph/0602142.

17. Thompson, C. & Duncan, R. C. Neutron star dynamos and the origins of pulsar magnetism. ApJ **408**, 194–217 (1993).

18. Zhang, B. & Yan, H. The Internal-collision-induced Magnetic Reconnection and Turbulence (ICMART) Model of Gamma-ray Bursts. ApJ **726**, 90 (2011). 1011.1197.

19. Dai, Z. G., Wang, X. Y., Wu, X. F. & Zhang, B. X-ray Flares from Postmerger Millisecond Pulsars. *Science* **311**, 1127–1129 (2006). astro-ph/0602525.

20. Thompson, C. & Duncan, R. C. The Giant Flare of 1998 August 27 from SGR 1900+14. II. Radiative Mechanism and Physical Constraints on the Source. ApJ **561**, 980–1005 (2001). astro-ph/0110675.

21. Evans, P. A. *et al.* Swift and NuSTAR observations of GW170817: Detection of a blue kilonova. *Science* **358**, 1565–1570 (2017). 1710.05437.

22. Yu, Y.-W., Zhang, B. & Gao, H. Bright "Merger-nova" from the Remnant of a Neutron Star Binary Merger: A Signature of a Newly Born, Massive, Millisecond Magnetar. ApJ **776**, L40 (2013). 1308.0876.

23. Kasen, D., Fernández, R. & Metzger, B. D. Kilonova light curves from the disc wind outflows of compact object mergers. MNRAS **450**, 1777–1786 (2015). 1411.3726.

24. Li, S.-Z., Liu, L.-D., Yu, Y.-W. & Zhang, B. What powered AT2017gfo associated with GW170817? *ArXiv e-prints* (2018). 1804.06597.

25. Metzger, B. D. & Piro, A. L. Optical and X-ray emission from stable millisecond magnetars formed from the merger of binary neutron stars. MNRAS **439**, 3916–3930 (2014). 1311.1519.

26. Kasen, D., Metzger, B., Barnes, J., Quataert, E. & Ramirez-Ruiz, E. Origin of the heavy elements in binary neutron-star mergers from a gravitational-wave event. Nature **551**, 80–84 (2017). 1710.05463.

27. Ruiz, M., Shapiro, S. L. & Tsokaros, A. GW170817, general relativistic magnetohydrodynamic simulations, and the neutron star maximum mass. Phys. Rev. D **97**, 021501 (2018). 1711.00473.

28. Demorest, P. B., Pennucci, T., Ransom, S. M., Roberts, M. S. E. & Hessels, J. W. T. A two-solar-mass neutron star measured using Shapiro delay. Nature **467**, 1081–1083 (2010). 1010.5788.

474 29. Lattimer, J. M. & Prakash, M. Neutron star observations: Prognosis for equation of state
475 constraints. Phys. Rep. **442**, 109–165 (2007). astro-ph/0612440.

476 30. Gao, H., Zhang, B. & Lü, H.-J. Constraints on binary neutron star merger product from short
477 GRB observations. Phys. Rev. D **93**, 044065 (2016). 1511.00753.

478 31. Schlafly, E. F. & Finkbeiner, D. P. Measuring Reddening with Sloan Digital Sky Survey Stellar
479 Spectra and Recalibrating SFD. ApJ **737**, 103 (2011). 1012.4804.

480 32. D'Avanzo, P. *et al.* The evolution of the X-ray afterglow emission of GW 170817 / GRB
481 170817A in XMM-Newton observations. *ArXiv e-prints* (2018). 1801.06164.

482 33. Haggard, D. *et al.* A Deep Chandra X-Ray Study of Neutron Star Coalescence GW170817.
483 ApJ **848**, L25 (2017). 1710.05852.

484 34. Lasker, B. M. *et al.* The Second-Generation Guide Star Catalog: Description and Properties.
485 AJ **136**, 735–766 (2008). 0807.2522.

486 35. Deustua, S. *WFC3 Data Handbook Version 3.0*.

487 36. Gonzaga, S., Hack, W., Fruchter, A. & Mack, J. *The DrizzlePac Handbook*.

488 37. Lyman, J. D. *et al.* The optical afterglow of the short gamma-ray burst associated with
489 GW170817. *ArXiv e-prints* (2018). 1801.02669.

490 38. Dobie, D. *et al.* A turnover in the radio light curve of GW170817. *ArXiv e-prints* (2018).
491 1803.06853.

39. Margutti, R. *et al.* The Binary Neutron Star Event LIGO/Virgo GW170817 160 Days after Merger: Synchrotron Emission across the Electromagnetic Spectrum. ApJ **856**, L18 (2018). 1801.03531.

40. Margutti, R. *et al.* X-ray flare candidates in short gamma-ray bursts. MNRAS **417**, 2144–2160 (2011). 1107.1740.

41. Lazzati, D. *et al.* Late time afterglow observations reveal a collimated relativistic jet in the ejecta of the binary neutron star merger GW170817. *ArXiv e-prints* (2017). 1712.03237.

42. Kathirgamaraju, A., Barniol Duran, R. & Giannios, D. Off-axis short GRBs from structured jets as counterparts to GW events. MNRAS **473**, L121–L125 (2018). 1708.07488.

43. Nakar, E., Gottlieb, O., Piran, T., Kasliwal, M. M. & Hallinan, G. From γ to Radio - The Electromagnetic Counterpart of GW 170817. *ArXiv e-prints* (2018). 1803.07595.

44. Foreman-Mackey, D., Hogg, D. W., Lang, D. & Goodman, J. emcee: The MCMC Hammer. PASP **125**, 306 (2013). 1202.3665.

45. Aloy, M. A., Janka, H.-T. & Müller, E. Relativistic outflows from remnants of compact object mergers and their viability for short gamma-ray bursts. A&A **436**, 273–311 (2005). astro-ph/0408291.

46. Sari, R., Piran, T. & Narayan, R. Spectra and Light Curves of Gamma-Ray Burst Afterglows. ApJ **497**, L17–L20 (1998). astro-ph/9712005.

510 47. Abbott, B. P. *et al.* A gravitational-wave standard siren measurement of the Hubble constant.
511 Nature **551**, 85–88 (2017). 1710.05835.

512 48. Riess, A. G. *et al.* A 2.4% Determination of the Local Value of the Hubble Constant. ApJ **826**,
513 56 (2016). 1604.01424.

514 49. Planck Collaboration *et al.* Planck 2015 results. XIII. Cosmological parameters. A&A **594**,
515 A13 (2016). 1502.01589.

516 50. Burrows, D. N. *et al.* Bright X-ray Flares in Gamma-Ray Burst Afterglows. *Science* **309**,
517 1833–1835 (2005). arXiv:astro-ph/0506130.

518 51. Piro, L. *et al.* Probing the Environment in Gamma-Ray Bursts: The Case of an X-Ray Pre-
519 cursor, Afterglow Late Onset, and Wind Versus Constant Density Profile in GRB 011121 and
520 GRB 011211. ApJ **623**, 314–324 (2005). astro-ph/0412589.

521 52. Nakar, E. & Granot, J. Smooth light curves from a bumpy ride: relativistic blast wave encoun-
522 ters a density jump. MNRAS **380**, 1744–1760 (2007). astro-ph/0606011.

523 53. Gat, I., van Eerten, H. & MacFadyen, A. No Flares from Gamma-Ray Burst Afterglow Blast
524 Waves Encountering Sudden Circumburst Density Change. ApJ **773**, 2 (2013). 1304.3415.

525 54. Uhm, Z. L. & Zhang, B. Dynamics and Afterglow Light Curves of Gamma-Ray Burst Blast
526 Waves Encountering a Density Bump or Void. ApJ **789**, 39 (2014). 1401.6758.

527 55. Branchini, E. *et al.* Studying the Warm Hot Intergalactic Medium with Gamma-Ray Bursts.
528 ApJ **697**, 328–344 (2009). 0903.1861.

529 56. Granot, J., Nakar, E. & Piran, T. Astrophysics: refreshed shocks from a γ-ray burst. Nature
530 **426**, 138–139 (2003). astro-ph/0304563.

531 57. Kumar, P. & Panaitescu, A. Afterglow Emission from Naked Gamma-Ray Bursts. ApJ **541**,
532 L51–L54 (2000). arXiv:astro-ph/0006317.

533 58. Yi, S.-X., Wu, X.-F., Wang, F.-Y. & Dai, Z.-G. Constraints on the Bulk Lorentz Factors of
534 GRB X-Ray Flares. ApJ **807**, 92 (2015). 1505.04233.

535 59. Deng, W., Li, H., Zhang, B. & Li, S. Relativistic MHD Simulations of Collision-induced
536 Magnetic Dissipation in Poynting-flux-dominated Jets/outflows. ApJ **805**, 163 (2015).
537 1501.07595.

538 60. Lazarian, A., Zhang, B. & Xu, S. Gamma-ray Bursts Induced by Turbulent Reconnection.
539 *ArXiv e-prints* (2018). 1801.04061.

540 61. Metzger, B. D., Thompson, T. A. & Quataert, E. A Magnetar Origin for the Kilonova Ejecta
541 in GW170817. ApJ **856**, 101 (2018). 1801.04286.

542 62. Margalit, B. & Metzger, B. D. Constraining the Maximum Mass of Neutron Stars from Multi-
543 messenger Observations of GW170817. ApJ **850**, L19 (2017). 1710.05938.

544 63. Yu, Y.-W. & Dai, Z.-G. A long-lived remnant neutron star after GW 170817 inferred from its
545 associated kilonova. *ArXiv e-prints: arXiv:1711.01898* (2017). 1711.01898.

546 64. Metzger, B. D., Quataert, E. & Thompson, T. A. Short-duration gamma-ray bursts with
547 extended emission from protomagnetar spin-down. MNRAS **385**, 1455–1460 (2008).
548 0712.1233.

549 65. Fan, Y.-Z., Wu, X.-F. & Wei, D.-M. Signature of gravitational wave radiation in afterglows of
550 short gamma-ray bursts? Phys. Rev. D **88**, 067304 (2013). 1302.3328.

551 66. Rowlinson, A., O'Brien, P. T., Metzger, B. D., Tanvir, N. R. & Levan, A. J. Signatures
552 of magnetar central engines in short GRB light curves. MNRAS **430**, 1061–1087 (2013).
553 1301.0629.

554 67. Lü, H.-J., Zhang, B., Lei, W.-H., Li, Y. & Lasky, P. D. The Millisecond Magnetar Central
555 Engine in Short GRBs. ApJ **805**, 89 (2015). 1501.02589.

556 68. Dai, Z. G. & Lu, T. Gamma-ray burst afterglows and evolution of postburst fireballs with
557 energy injection from strongly magnetic millisecond pulsars. A&A **333**, L87–L90 (1998).
558 arXiv:astro-ph/9810402.

559 69. Zhang, B. & Mészáros, P. Gamma-Ray Burst Afterglow with Continuous Energy Injec-
560 tion: Signature of a Highly Magnetized Millisecond Pulsar. ApJ **552**, L35–L38 (2001).
561 arXiv:astro-ph/0011133.

562 70. Geng, J.-J. *et al.* Brightening X-Ray/Optical/Radio Emission of GW170817/SGRB 170817A:
563 Evidence for an Electron-Positron Wind from the Central Engine? ApJ **856**, L33 (2018).
564 1803.07219.